

Detection of Diffuse Hot Gas Around the Young, Potential Superstar Cluster H72.97–69.39

TRINITY L. WEBB,¹ JENNIFER A. RODRIGUEZ,¹

THESE AUTHORS CONTRIBUTED EQUALLY TO THIS WORK.

LAURA A. LOPEZ,^{1,2,3} ANNA L. ROSEN,^{4,5} LACHLAN LANCASTER,^{6,3,*} OMNARAYANI NAYAK,⁷ ANNA F. MCLEOD,^{8,9}
PAARMITA PANDEY,^{1,2} GRACE M. OLIVIER¹⁰

¹*Department of Astronomy, The Ohio State University, 140 W. 18th Ave., Columbus, OH 43210, USA*

²*Center for Cosmology and AstroParticle Physics, The Ohio State University, 191 W. Woodruff Ave., Columbus, OH 43210, USA*

³*Center for Computational Astrophysics, Flatiron Institute, 162 5th Avenue, New York, NY 10010, USA*

⁴*Department of Astronomy, San Diego State University, 5500 Campanile Dr, San Diego, CA 92182, USA*

⁵*Computational Science Research Center, San Diego State University, 5500 Campanile Dr, San Diego, CA 92182, USA*

⁶*Department of Astronomy, Columbia University, 550 W 120th St, New York, NY 10025, USA*

⁷*Space Telescope Science Institute, 3700 San Martin Drive, Baltimore, MD 21218, USA*

⁸*Centre for Extragalactic Astronomy, Department of Physics, Durham University, South Road, Durham DH1 3LE, UK*

⁹*Institute for Computational Cosmology, Department of Physics, University of Durham, South Road, Durham DH1 3LE, UK*

¹⁰*Department of Physics and Astronomy and George P. and Cynthia Woods Mitchell Institute for Fundamental Physics and Astronomy, Texas A&M University, 4242 TAMU, College Station, TX 77843-4242 USA*

ABSTRACT

We present the first Chandra X-ray observations of H72.97–69.39, a highly-embedded, potential super-star cluster (SSC) in its infancy located in the star-forming complex N79 of the Large Magellanic Cloud. We detect particularly hard, diffuse X-ray emission that is coincident with the young stellar objects (YSOs) identified with JWST, and the hot gas fills cavities in the dense gas mapped by ALMA. The X-ray spectra are best fit with either a thermal plasma or power-law model, and assuming the former, we show that the X-ray luminosity of $L_X = (1.0 \pm 0.3) \times 10^{34}$ erg s⁻¹ is a factor of ~ 20 below the expectation for a fully-confined wind bubble. Our results suggest that stellar wind feedback produces diffuse hot gas in the earliest stages of massive star cluster formation and that wind energy can be lost quickly via either turbulent mixing followed by radiative cooling or by physical leakage.

Keywords: Young star clusters — HII regions — Stellar wind bubbles

1. INTRODUCTION

Massive stars are born in clustered environments (Krumholz et al. 2019), depositing substantial energy and momentum to the surrounding interstellar medium (ISM) through a variety of feedback mechanisms. In particular, fast, line-driven stellar winds (with velocities of $v_w \sim 10^3$ km s⁻¹) sweep up surrounding gas and create low-density cavities shock-heated to $\sim 10^7$ K temperatures (Castor et al. 1975; Weaver et al. 1977; Cantó et al. 2000; Stevens & Hartwell 2003; Harper-Clark & Murray 2009). Diffuse X-ray emission associated with these fast stellar winds has been detected from numerous massive star clusters (MSCs) in the Milky Way (Moffat et al. 2002; Yusef-Zadeh et al. 2002; Townsley et al. 2003;

Muno et al. 2006; Townsley et al. 2011) and the Magellanic Clouds (Townsley et al. 2006; Lopez et al. 2011, 2014). Although the integrated kinetic energy carried in the stellar winds is comparable to the kinetic energy delivered by supernova explosions (Agertz et al. 2013), the actual dynamical impact of the stellar wind feedback and how it evolves over time remains uncertain.

One open issue is the role of winds in the early evolution of MSCs, and the study of young, embedded sources can provide important insights. Toward this end, the highly embedded N79 star-forming complex in the southwestern region of the Large Magellanic Cloud (LMC; see Figure 1), which has a star-formation efficiency of ~ 2 times that of the starburst region 30 Doradus (hereafter 30 Dor; Ochsendorf et al. 2017), is an ideal target to study the role of stellar wind feedback at the onset of star cluster formation. The N79 region has several CO sub-complexes spanning ~ 500 pc (see Figure 1; Wong et al. 2011; Ochsendorf et al. 2017) and harbors a newly forming (< 0.5 Myr old; Ochsendorf

Corresponding author: Trinity Webb
webb.916@osu.edu

* Simons Fellow

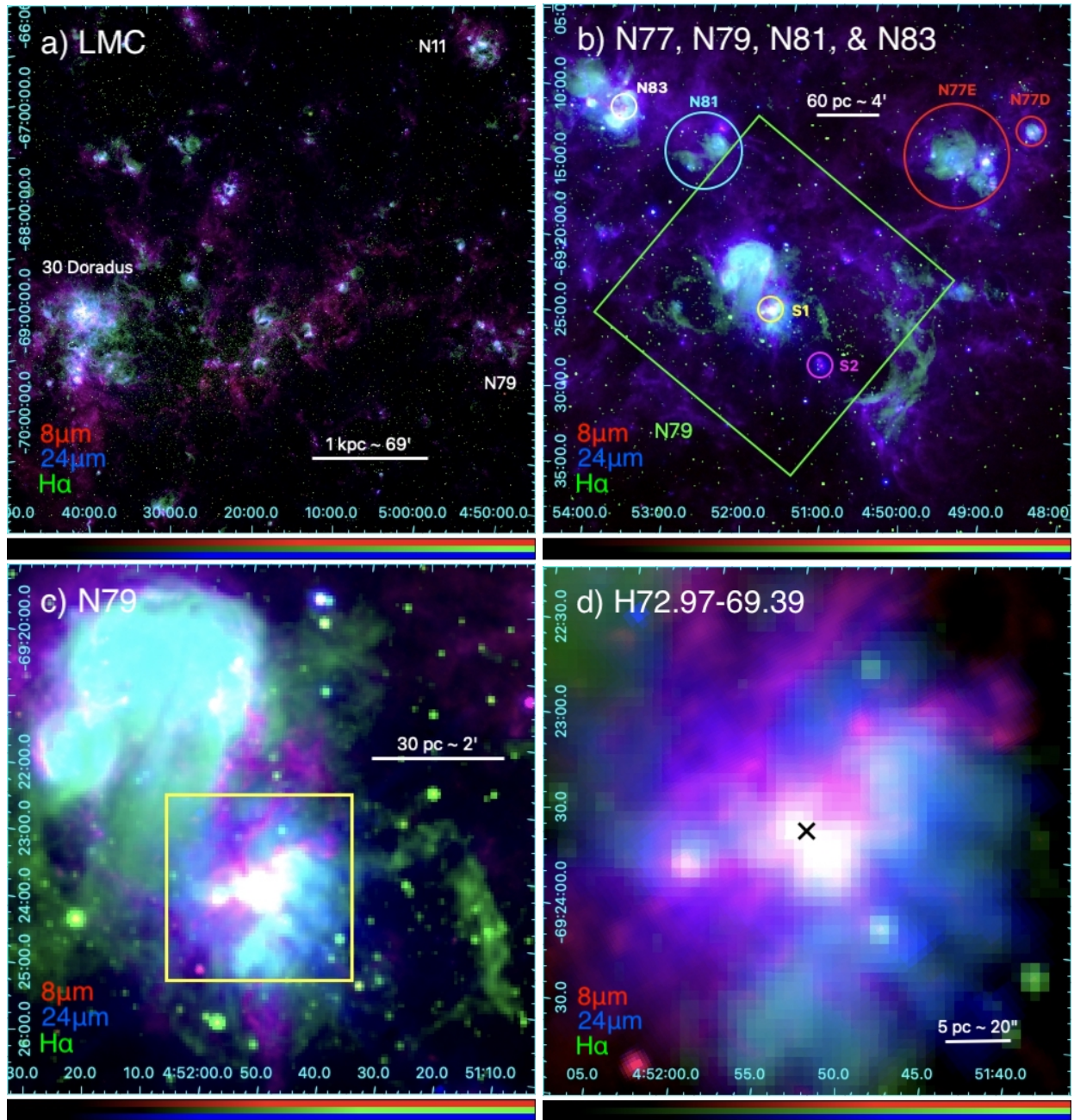


Figure 1. Three-color images, with Spitzer SAGE $8\mu\text{m}$ in red, Spitzer SAGE $24\mu\text{m}$ in blue (Meixner et al. 2006), and $\text{H}\alpha$ in green (Smith & MCELS Team 1998). North is up, East is left. (a) Large-scale, three-color image of the Large Magellanic Cloud. (b) Zoomed in three-color image of N77, N79, N81, and N83 identified by Henize (1956). N79, N83, and N77 have also been referred to as N79 South, N79 East, and N79 West in Ochsendorf et al. (2017), respectively. Two Spitzer-identified clusters of young stellar objects (YSOs) within N79 are circled in yellow (the location of H72.97–69.39) and magenta, known as N79S1 and N79S2, respectively (Nayak et al. 2024). The green box surrounding N79 is the field of view of the Chandra ACIS-I observations. (c) Zoomed in three-color image of N79. The yellow box indicates the area surrounding H72.97–69.39 as shown in panel d. (d) Zoomed in three-color image in the vicinity of H72.97–69.39 (black X).

et al. 2017), potential proto-superstar cluster (SSC) H72.97–69.39¹ based on its inferred bolometric luminosity ($\sim 2 \times 10^6 L_\odot$) and accelerating star-formation rate (Seale et al. 2014; Ochsendorf et al. 2017; Nayak et al. 2019). In comparison, R136 (the star cluster powering 30 Dor) has a luminosity of $\sim 7.8 \times 10^7 L_\odot$ (Malumuth & Heap 1994) and a decelerating star-formation rate. Both 30 Dor and N79 are on opposite leading edges of the LMC’s spiral arms (Ochsendorf et al. 2017), possibly facilitating their starburst activity due to large-scale dynamical inflows along the tidal tails. While R136 is 2 Myr old (Hunter et al. 1995), H72.97–69.39 is in the earliest stages of formation, offering an interesting point of comparison.

Previous studies of H72.97–69.39 have mapped the N79 star-forming complex in optical, infrared, and sub-mm wavelengths (Ochsendorf et al. 2017; Nayak et al. 2019, 2024), tracing the young stars, the cold molecular gas, and the dust. Here we study the X-ray emission of H72.97–69.39 with the Chandra X-ray Observatory, and we explore stellar-wind feedback at an early stage ($\lesssim 0.5$ Myr) in star formation. Specifically, we show the spatial distribution of the hot gas relative to the other gas phases, dust, and stars as well as compare the X-ray luminosity and hot-gas temperature predictions from wind bubble models. For comparison, the sample of 32 HII regions (including the full N79-South complex) examined by Lopez et al. (2014) had estimated ages of 3 – 10 Myr, when the sources’ shells had expanded $\sim 4 - 150$ pc. The other SSC in the LMC, R136 in 30 Dor, has been observed extensively by Chandra, including an X-ray Visionary Project (PI: L. Townsley) totaling ~ 2 Ms (Townsley et al. 2024). Chandra studies of 30 Dor have found diffuse, hot gas filling the five H α shells of the region, producing a total X-ray luminosity of $L_X = 4.5 \times 10^{36}$ erg s⁻¹ from the diffuse emission in the 0.2–2.0 keV band (Townsley et al. 2006; Lopez et al. 2011).

This paper is structured as follows. In Section 2, we describe the new Chandra observations of H72.97–69.39 and discuss the analysis to produce the X-ray images and spectra. In Section 3, we present the results, including the spatial extent, the nature, and the association of the X-ray emission with young stellar objects (YSOs) and anti-coincidence with the dense gas. In Section 4.1, we interpret the results in the context of wind bubble models, and in Section 4.2, we compare the X-ray emission of H72.97–69.39 to other Milky Way and LMC sources (by comparison, most SMC HII regions are

Table 1. Detected Counts Per Band in Source and Background Regions^a

Band	Source	Background	Net
	Counts	Counts	Counts
Broad (0.5–7.0 keV)	558±24	805±28	156±28
Soft (0.5–1.2 keV)	75±9	147±12	2 ⁺¹¹ ₋₂
Medium (1.2–2.0 keV)	128±11	147±12	54±13
Hard (2.0–7.0 keV)	355±19	548±23	81±22

^aThe source and background regions have areas of 14875 pixel² (~ 3600 arcsec²) and 29742 pixel² (~ 7200 arcsec²), respectively.

not X-ray detected; Lopez et al. 2014). We conclude in Section 5.

2. DATA ANALYSIS

2.1. Imaging

H72.97–69.39 in N79 was observed three times with Chandra ACIS-I in July 2021 for a total of 98 ks (ObsIDs 22473 [29 ks], 23062 [39 ks], and 25091 [30 ks]). These Chandra datasets, obtained by the Chandra X-ray Observatory, are contained in [doi:10.25574/cdc.292](https://doi.org/10.25574/cdc.292). Data were reprocessed and reduced using Chandra Interactive Analysis of Observations CIAO version 4.15 (Fruscione et al. 2006). We used the *merge_obs* function to produce exposure-corrected images (images that are normalized by the effective area across the detectors) in the soft (0.5–1.2 keV), medium (1.2–2.0 keV), hard (2.0–7.0 keV), and broad (0.5–7.0 keV) energy bands (see Figure 2). We detect 156 ± 28 net, background-subtracted, broad-band counts within a $1' \times 1'$ area surrounding H72.97–69.39 in the merged, broad-band image. Background subtraction was performed using the regions shown in Figure 3, and the total source and background counts in each band are listed in Table 1. The source region is not statistically significantly detected above the background in the soft (0.5–1.2 keV) band, and the signal is strongest in the hard (2.0–7.0 keV) X-ray band.

2.2. Spectroscopy

In addition to the imaging analysis, we conduct a spectral analysis of the X-rays from H72.97–69.39. Using the CIAO command *specextract*, we extracted spectra from a source region with an area of $1' \times 1'$ (see Figure 3). The background spectra were extracted from two $1' \times 1'$ regions to the south $\sim 6'$ of the source region. Background regions were selected to avoid X-ray point sources identified with the CIAO command *wavdetect* and to not coincide with any bright 24 μ m emission.

¹ This source is catalogued as HSOBMHERICC J72.971176–69.391112 (Seale et al. 2014, ; hereafter H72.97–69.39) and will be referred to as H72.97–69.39 throughout this paper. The position of H72.97–69.39 was refined by Nayak et al. (2019) based on the compact core’s continuum emission to R.A. 72.972201 and decl. -69.391301 .

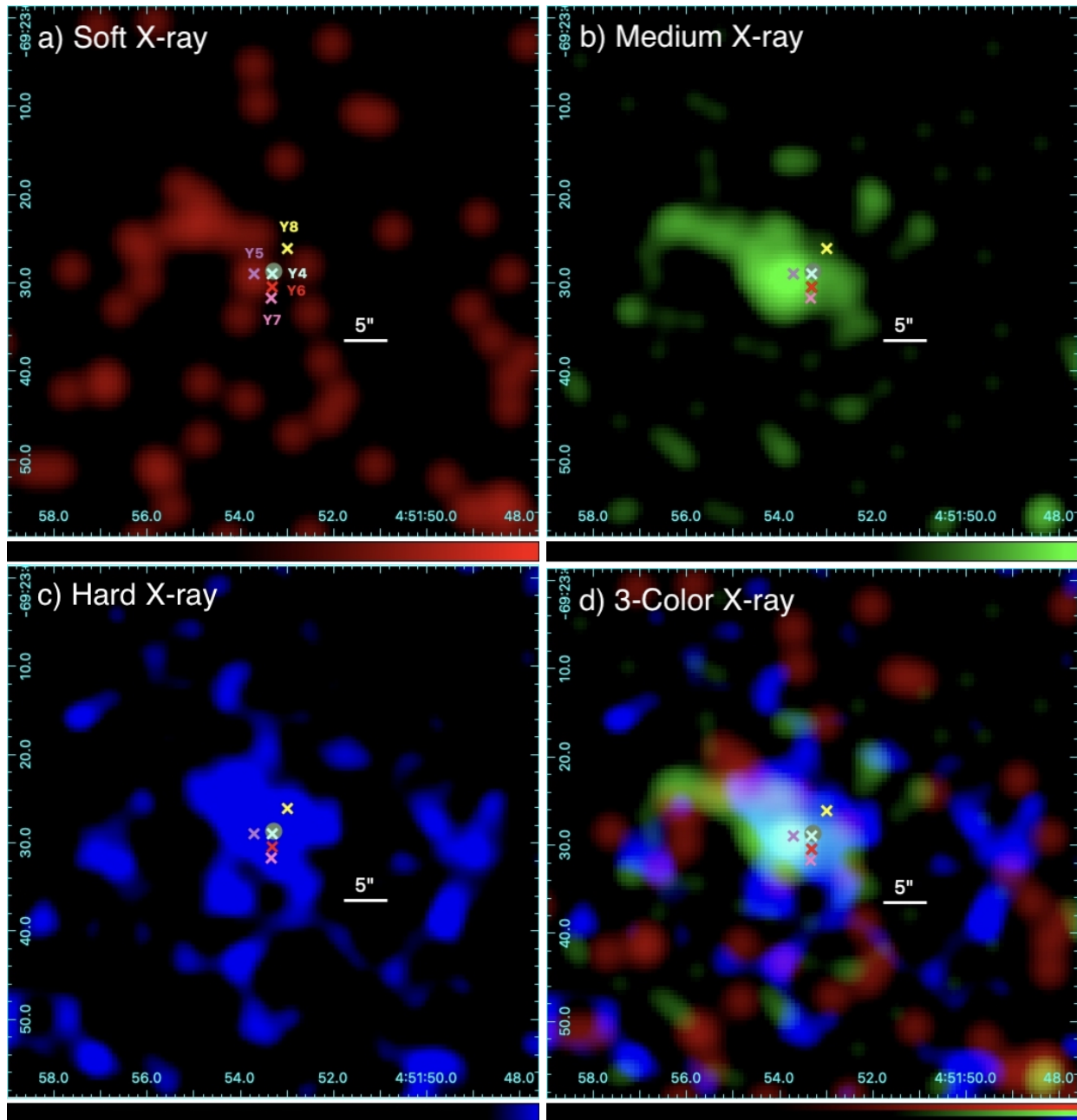


Figure 2. X-ray images of H72.97–69.39 in soft [0.5 – 1.2 keV] (a), medium [1.2 – 2.0 keV] (b), hard [2.0 – 7.0 keV] (c), and broad band [0.5 – 7.0 keV] (d). The scale bar is $5'' \approx 1.2$ pc, and the images are $1' \times 1'$ in size. A gray circle marks the position of H72.97–69.39, and five YSOs identified by [Nayak et al. \(2024\)](#) with JWST MRS data are labeled with X symbols. North is up, East is left. The X-ray emission is extended $\approx 10''$ and peaks $\approx 5''$ offset from the position of H72.97–69.39.

We jointly fit the spectra using either thermal or non-thermal plasma models in XSPEC version 12.13.0c ([Arnaud 1996](#)). The best fit parameters for these models can be seen in Table 2. The thermal plasma model included a multiplicative constant (CONST), two absorption components (PHABS*VPHABS), and one additive thermal plasma component (APEC). The CONST component was allowed to vary to account for the slight variations in flux between the three observations. The PHABS

component is a photoelectric absorption of $M(E) = \exp[-\eta_{\text{H}}\sigma(E)]$, where $\sigma(E)$ is the photo-electric cross-section and $\eta_{\text{H}}(E)$ is the equivalent hydrogen column². We fixed the first PHABS to account for the column density of the Milky Way and set it to the neutral atomic hydrogen (HI) density observed in the direction of N79,

² See heasarc.gsfc.nasa.gov/xanadu/xspec/manual/XSmodelPhabs.html

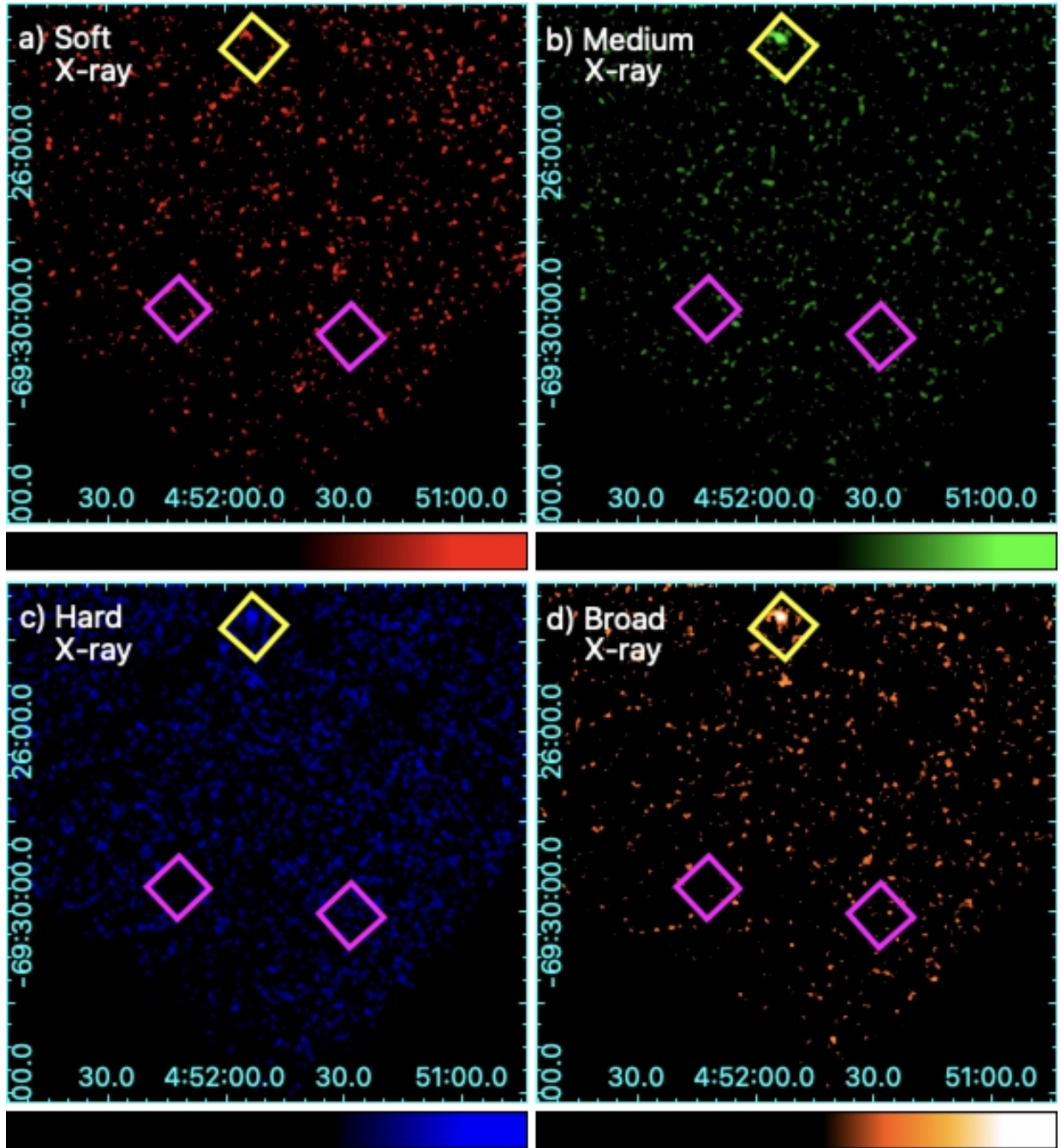


Figure 3. Zoomed in Chandra ACIS-I images showing the source region (yellow box) and background regions (magenta boxes) used to create spectra of H72.97–69.39. Each region is $1' \times 1'$. The distance from the center of the source region to the center of the left-hand background region is $\approx 6.0'$ (≈ 87.5 pc), and the distance to the right-hand background region is $\approx 6.7'$ (≈ 98.1 pc). Panel (a) shows the soft [0.5 – 1.2 keV] X-ray band in red, panel (b) shows the medium [1.2 – 2.0 keV] in green, panel (c) shows the hard [2.0 – 7.0 keV] in blue, and panel (d) shows the broad-band [0.5 – 7.0 keV] in orange.

$N_{\text{H}}^{\text{MW}} = 3.24 \times 10^{21} \text{ cm}^{-2}$ (HI4PI Collaboration et al. 2016). By adopting this value, we neglect the contribution from the molecular and ionized components to the hydrogen column density. We note that Wilms et al. (2000) found that atomic hydrogen is responsible for $\sim 80\%$ of the total hydrogen column density, and our selected N_{H}^{MW} is comparable to the total hydrogen column density of $N_{\text{H,tot}} = 3.42 \times 10^{21} \text{ cm}^{-2}$ derived from Willingale et al. (2013), assuming uniform elemental abundances and $N_{\text{H,tot}} = N_{\text{HI}} + 2N_{\text{H}_2}$, with the atomic hydrogen column density N_{HI} derived from 21-cm radio observations and the molecular hydrogen column density N_{H_2} from X-ray afterglows of gamma-ray bursts (GRBs).

The VPHABS component represented the column density of the LMC toward H72.97–69.39 and was set to $N_{\text{H}}^{\text{LMC}} = 5.5 \times 10^{21} \text{ cm}^{-2}$, the upper-limit value defined by the XSPEC ERROR command when $N_{\text{H}}^{\text{LMC}}$ was allowed to vary. The APEC component, reflecting an optically thin thermal plasma, is defined by its temperature kT , metal abundances, redshift, and a normalization factor. Solar abundances were adopted from Asplund et al. (2009). The abund command in XSPEC³ was used to set the abundance to 0.5 solar metallicity in the APEC and VPHABS components to match the values of the LMC ISM (Kurt & Dufour 1998; Maggi et al. 2016). The temperature and normalization were allowed to vary in the fits.

For comparison, we also tried fitting the data with a power-law component (POWERLAW) representing non-thermal emission in the place of the APEC component. Given the low signal (156 net broad-band counts), we did not attempt a spectral model that included both thermal and non-thermal components as it would be under-constraining (i.e., too many free parameters for the limited degrees of freedom).

3. RESULTS

Figure 2 shows the exposure-corrected, three-color X-ray image of the soft (0.5 – 1.2 keV), medium (1.2 – 2.0 keV), and hard (2.0 – 7.0 keV) X-ray bands around H72.97–69.39. The X-rays are spatially extended $\sim 10'' \approx 2.4 \text{ pc}$ in radius, much greater than the $\approx 0.5''$ on-axis point spread function (PSF) of Chandra ACIS⁴. The peak of the X-rays is spatially offset $\approx 5'' \approx 1.2 \text{ pc}$ east of the star cluster. It is possible that some emission arises from unresolved point sources coincident with the diffusion emission, but no resolved point sources are apparent in the vicinity of H72.97–69.39.

The X-rays (particularly the medium and hard bands) are spatially coincident with five YSOs (identified as Y4, Y5, Y6, Y7, and Y8) identified with recent JWST MRS observations (Nayak et al. 2024), as marked in Figure 2.

Y4 is coincident with H72.97–69.39, and it is the only one of the five YSOs without emission lines associated with polycyclic aromatic hydrocarbons (PAHs) in the MRS spectra, likely stemming from ionizing radiation destroying surrounding PAHs (e.g., Madden et al. 2006; Gordon et al. 2008; Montillaud et al. 2013; Egorov et al. 2023). Y5 is located at the peak of the broad-band X-ray emission and is the only YSO that coincides with soft X-rays. All five YSOs coincide with hard X-ray emission. While their physical association with the hard X-rays is not entirely certain, it is possible that they arise from colliding stellar winds in binary systems (Rauw & Nazé 2016). All except Y8 have coincident medium X-ray emission.

To quantify the spatial distribution of the X-ray emission, we measured the background-subtracted surface brightness of the soft, medium, and hard X-ray bands from three annuli centered on H72.97–69.39 with radii of $5'' (\approx 1.2 \text{ pc})$, $10'' (\approx 2.4 \text{ pc})$, and $15'' (\approx 3.6 \text{ pc})$; see Figure 4) and produced the profiles plotted in Figure 5. We find that the hard X-rays have the highest net surface brightness near H72.97–69.39, while the medium and hard X-ray surface brightnesses are comparable at radii of 2.4 pc and 3.6 pc. These profiles suggest that the X-ray emission is hardest around H72.97–69.39 and softens with distance from the star cluster. X-ray hardness variations across the region may reflect higher column densities $N_{\text{H}}^{\text{LMC}}$ that are absorbing softer X-rays, elevated hot gas temperatures kT producing more hard X-rays, and/or the presence of colliding-wind massive binaries (Rauw & Nazé 2016).

In Figure 4, we compare the broad-band X-ray emission with the ^{13}CO maps (Nayak et al. 2019) and the DeMCELS $\text{H}\alpha$ data (Points et al. 2024). The X-rays appear to fill the low-density cavities where the ^{13}CO is dim. The $\text{H}\alpha$ is coincident with the X-ray emission surrounding H72.97–69.39 and the YSOs from Nayak et al. (2024), revealing a bubble that is filled with hot gas, producing the X-ray emission.

Although our Chandra program targeted H72.97–69.39, N79S2 (see Figure 1) – another part of N79 South observed with JWST MRS by Nayak et al. (2024) – was also in the field of view. In Figure 6, we show the three-color X-ray image of N79S2. We detect 12 ± 5 net, broad-band counts that are coincident with the three YSOs Y9, Y10, and Y11 identified by Nayak et al. (2024). In particular, the hard X-rays are concentrated to the location of Y11. The angular extent of the emission, $\sim 5''$, is consistent with the off-axis PSF of Chandra, and thus, we are unable to distinguish whether the emission is point-like or diffuse in nature.

The X-ray spectra from H72.97–69.39 (shown in Figure 7) give additional constraints on the emission. Both the single thermal plasma model and the power-law model yield statistically good fits (see Table 2). We find an upper-limit on the LMC column density toward the source of $N_{\text{H}}^{\text{LMC}} = 5.5 \times 10^{21} \text{ cm}^{-2}$, and we fixed

³ <https://heasarc.gsfc.nasa.gov/xanadu/xspec/manual/node116.html>

⁴ <https://cxc.harvard.edu/proposer/POG/html/chap6.html>

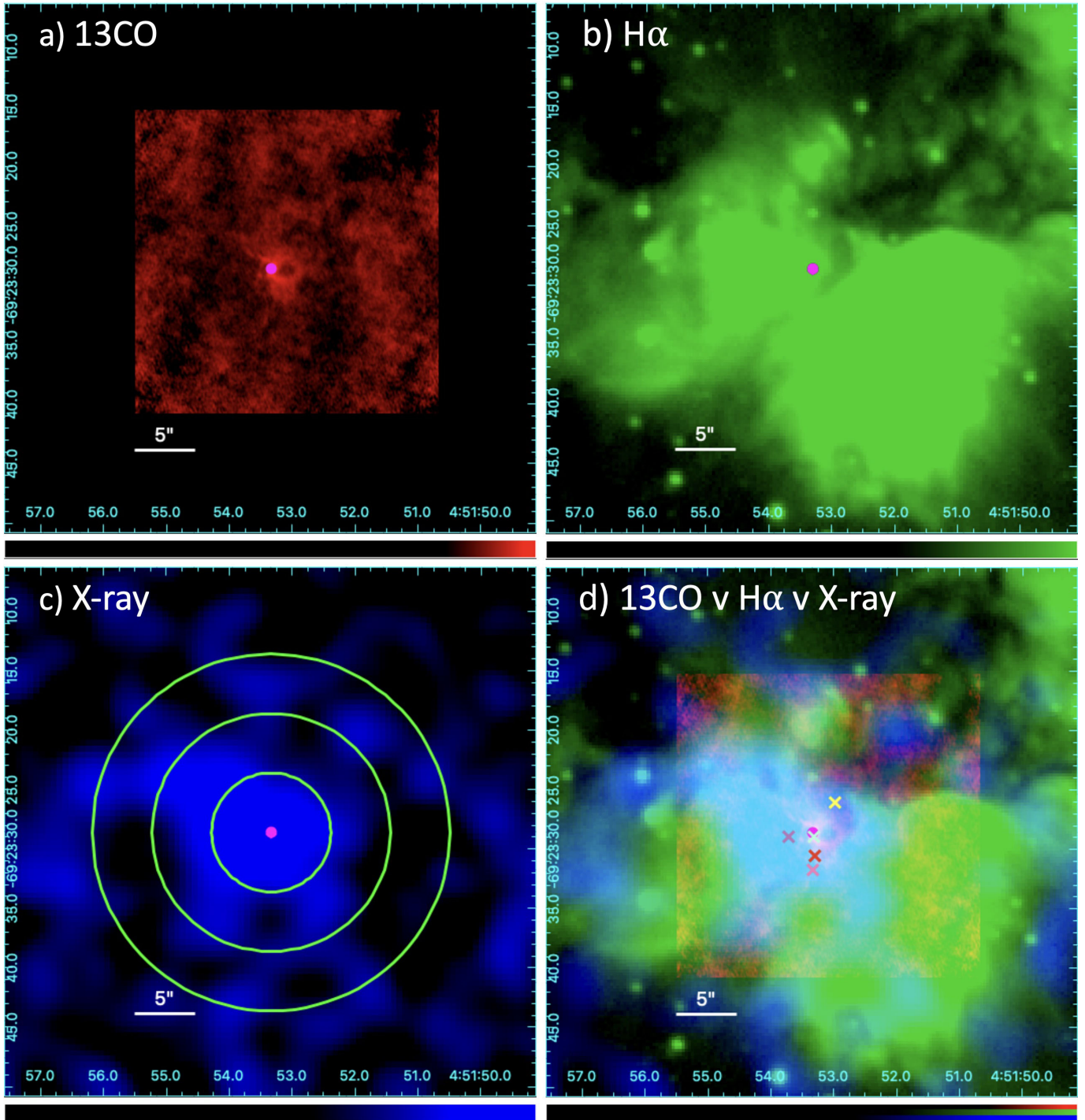


Figure 4. Comparison of the (a) ^{13}CO emission observed with ALMA in red by Nayak et al. (2019) with the (b) DeMCELS $\text{H}\alpha$ emission from Points et al. (2024) in green and (c) Chandra broad-band (0.5 – 7.0 keV) X-ray emission in blue. The five YSOs identified with JWST by Nayak et al. (2024) are marked with Xs in panel (d). H72.97–69.39 is denoted by a magenta circle in all panels. The diffuse X-rays appear to fill the low-density cavities where ^{13}CO is dim. Annuli in panel (c) were used to produce the multi-band surface-brightness profiles in Figure 5. All images are $0.75' \times 0.75'$ in size, and the scale bar is $5'' \approx 1.2$ pc at the distance of the LMC.

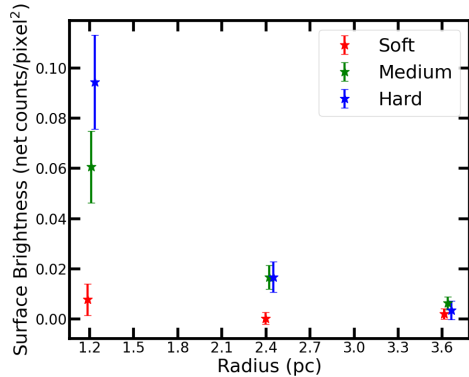


Figure 5. Background-subtracted, surface-brightness profile (in units of net counts pixel⁻²) of the soft (red), medium (green), and hard (blue) X-ray bands for the three annuli in Figure 4a. The hard X-rays have the greatest surface brightness near H72.97–69.39, and the medium and hard X-rays have comparable surface brightnesses at radii $\gtrsim 2.4$ pc. The soft X-rays are not statistically significantly detected in any annulus.

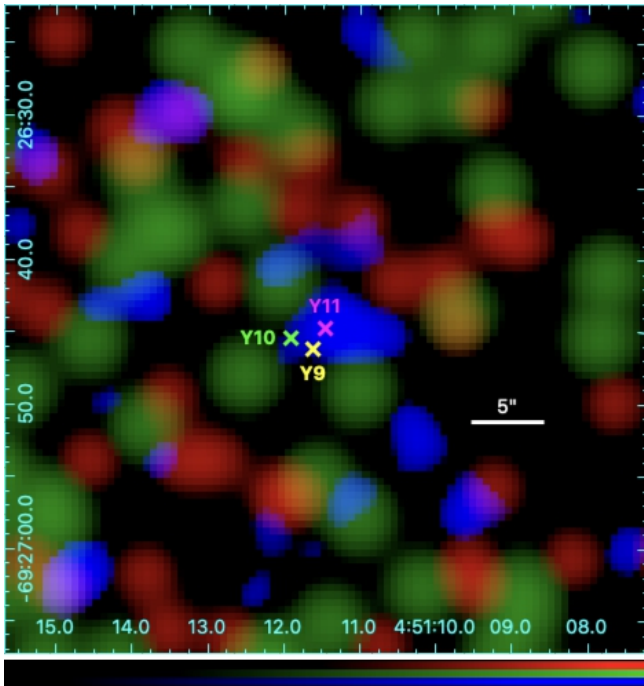


Figure 6. Three-color X-ray image of N79S2, where the soft X-rays (0.5–1.2 keV) are in red, medium X-rays (1.2–2 keV) are in green, and hard X-rays (2–7 keV) are in blue. The three YSOs identified with the JWST MRS data from Nayak et al. (2024) are labeled. The hard X-rays dominate this source, likely because of high absorbing column toward it. The image is $0.75' \times 0.75'$; the scale bar is $5'' \approx 1.2$ pc at the distance of the LMC.

it to this value before estimating the other parameters. The thermal plasma model gave a $\chi^2/\text{d.o.f.} = 54/52 = 1.04$ and a best-fit $kT = 3.5^{+32.1}_{-2.2}$ keV. The power-law model produces similar results, with a $\chi^2/\text{d.o.f.} = 53/47 = 1.15$ and a best-fit photon index of $\Gamma = 2.2^{+0.3}_{-0.6}$. The resultant luminosities for the two models are comparable and were $L_X = (1.0 \pm 0.3) \times 10^{34}$ erg s⁻¹ and $L_X = (1.2 \pm 0.3) \times 10^{34}$ erg s⁻¹, respectively.

4. DISCUSSION

In Section 3, we found that H72.97–69.39 (and the associated YSOs identified with JWST) has coincident diffuse X-ray emission. The flux in the medium and hard bands is more centrally concentrated than the soft X-rays, and the X-ray spectrum can be modeled as a thermal plasma or with a power-law. In Section 4.1, we compare these results to predictions from wind models, and in Section 4.2, we discuss how the X-ray properties of H72.97–69.39 compare to those of other young MSCs in the Milky Way and LMC.

4.1. Comparison to Wind Models X-ray Predictions

In an idealized HII region powered by a MSC, wind energy is injected at a rate of

$$L_w = \sum_{i=1}^N \frac{1}{2} \dot{M}_{w,i} v_{w,i}^2, \quad (1)$$

where $\dot{M}_{w,i}$ and $v_{w,i}$ are the mass-loss rate and wind velocity for individual stars i that are summed over the total N stars in the cluster. Typical values of L_w for Milky Way and LMC MSCs are $L_w \sim 10^{37} - 10^{39}$ erg s⁻¹ (e.g., Smith 2006; Rosen et al. 2014). We can estimate L_w for H72.97–69.39 assuming $L_{\text{bol}} = 2.2 \times 10^6 L_\odot$ (Ochsendorf et al. 2017) and relating it to the expected total wind luminosity using stellar population synthesis and a prescription for wind mass loss and velocity.

In particular, we first download isochrones of $[\text{Fe}/\text{H}] = -0.25$ (meant to approximate $Z = 0.5Z_\odot$, the LMC ISM metallicity: Kurt & Dufour 1998; Maggi et al. 2016) from the MIST⁵ database (Choi et al. 2016; Dotter 2016). We then generate a large (total mass $10^6 M_\odot$) sample of masses following the Kroupa IMF (Kroupa 2001) with minimum and maximum masses of $M_{\text{min}} = 0.01 M_\odot$ and $M_{\text{max}} = 200 M_\odot$. We use the MIST isochrones to derive bolometric luminosities for each star in the sample as a function of time. Assuming the mass-loss rates of Vink et al. (2000, 2001), we also calculate the wind mass loss and wind velocities of all stars with mass $M_* > 8 M_\odot$ in the sample and use Equation 1 to calculate their wind luminosities.

At each point in time (time-steps determined by the age steps of the MIST isochrones), we sum the bolometric and mechanical wind luminosities over all stars in

⁵ <https://waps.cfa.harvard.edu/MIST/>

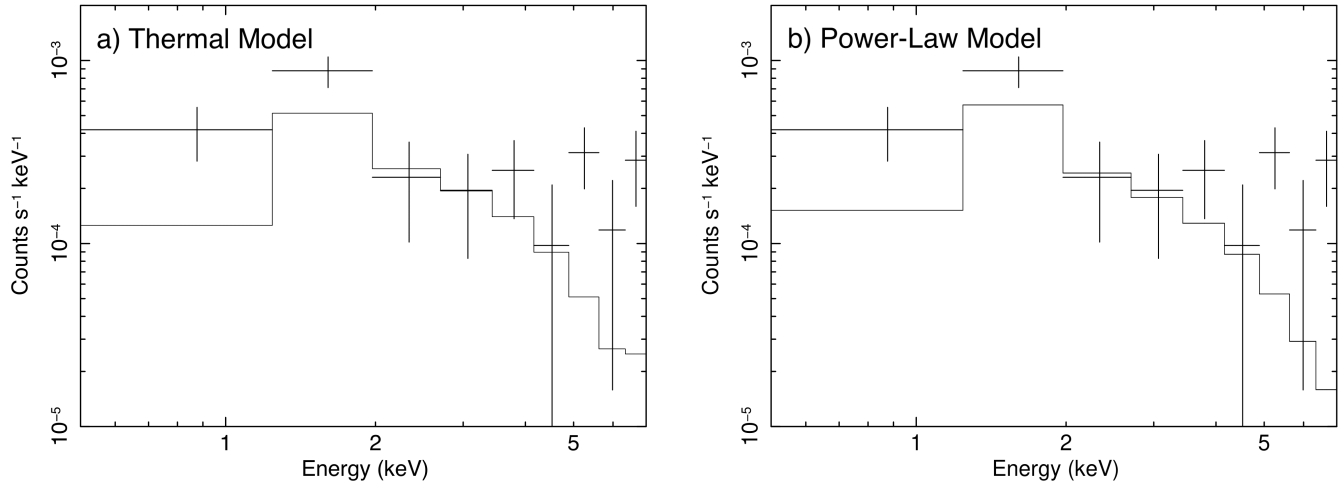


Figure 7. Extracted, background-subtracted spectra from a $1' \times 1'$ region around H72.97–69.39 with the best-fit thermal plasma model (a) and power-law model (b) overplotted. The best-fit parameters are listed in Table 2. Both models produce statistically good fits and predict similar X-ray luminosities from the source.

Table 2. Spectral Model Results

Model	kT (keV)	Γ	$\chi^2/\text{d.o.f.}$	Absorbed Flux ^a (erg cm ⁻² s ⁻¹)	Emitted Flux ^a (erg cm ⁻² s ⁻¹)	Luminosity (erg s ⁻¹)
Thermal Plasma	$3.5^{+32.1}_{-2.2}$	–	54/52	$(2.3 \pm 0.7) \times 10^{-14}$	$(3.4 \pm 1.0) \times 10^{-14}$	$(1.0 \pm 0.3) \times 10^{34}$
Power Law	–	$2.2^{+0.3}_{-0.6}$	53/47	$(2.2 \pm 0.6) \times 10^{-14}$	$(3.9 \pm 1.1) \times 10^{-14}$	$(1.2 \pm 0.3) \times 10^{34}$

^aAbsorbed fluxes are for the 0.5–7.0 keV band adopting a LMC and Milky Way column density of $N_{\text{H}}^{\text{LMC}} = 5.5 \times 10^{21} \text{ cm}^{-2}$ and $N_{\text{H}} = 3.24 \times 10^{21} \text{ cm}^{-2}$, respectively. Emitted fluxes are the unabsorbed fluxes in the same energy bands.

the sample and divide by the total mass of the sample to arrive at population-averaged values for L_{bol}/M_* and L_{w}/M_* . We average these ratios over ages < 2 Myr, roughly the period over which wind luminosities remain roughly constant before the onset of SNe (Lancaster et al. 2021a). We obtain $L_{\text{bol}}/M_* = 1.37 \times 10^3 L_{\odot}/M_{\odot}$ and $L_{\text{w}}/M_* = 4.20 L_{\odot}/M_{\odot}$. Given the L_{bol} of H72.97–69.39, we estimate a mechanical wind luminosity of $L_{\text{w}} = 6.7 \times 10^3 L_{\odot} = 2.6 \times 10^{37} \text{ erg s}^{-1}$.

In order to relate this value to an expected X-ray luminosity L_{X} in the bubble, we need to consult a model for wind-blown bubble evolution. The theoretical models of Castor et al. (1975) and Weaver et al. (1977) predict X-ray luminosities assuming the shock-heated gas is confined by a cool shell of swept-up ISM. Additionally, this cool shell is heated by the bubble’s hot gas through thermal conduction, resulting in evaporation and mass loading of the bubble interior, resulting in higher X-ray luminosities. An alternative model by Chevalier & Clegg (1985) ignores the surrounding ISM and assumes a steady, freely-expanding wind, equivalent to assuming that the “free-wind” of the Weaver et al. (1977) model

occupies the entire bubble volume. As the Castor and Weaver models can over-predict X-ray luminosity and Chevalier & Clegg can under-predict it, Harper-Clark & Murray (2009) introduced an intermediate model, where hot gas expands into an inhomogeneous ISM, creating a porous shell from which hot gas can escape/leak. Leakage is one mechanism by which energy can be lost from bubbles producing lower-than-expected X-ray luminosities (e.g., Lopez et al. 2011; Rosen et al. 2014). Other mechanisms have been proposed as possible sinks for the wind energy, chiefly turbulent mixing with the surrounding gas followed by radiative cooling (Rosen et al. 2014; Lancaster et al. 2021b; Rosen 2022).

The differences between these wind energy loss channels are likely dependent on the detailed density and temperature structure in the bubble’s interior, particularly at its interface. Here we simply present the predictions for X-ray luminosity L_{X} and radius R assuming a single density and temperature as predicted for a Weaver et al. (1977) model. The Weaver et al. model requires an assumption of the background number density of the surrounding cloud; measurements from

Ochsendorf et al. (2017) indicate a molecular gas mass $M_{\text{gas,H}_2} \approx 10^5 M_\odot$ within $R = 10^{1.4} \text{ pc} \approx 25 \text{ pc}$ (see their Figure 5). In the same region atomic gas contributes about one-third as much mass and ionized gas contributes negligibly, indicating an average gas mass density of $\rho \approx 2 M_\odot \text{ pc}^{-3} = 1.4 \times 10^{-22} \text{ g cm}^{-3}$.

Assuming an X-ray extent of $10'' \approx 2.4 \text{ pc}$ (Section 3) is the radius of the wind bubble R_b , we can use the Weaver et al. (1977) model to estimate the bubble age t , the predicted temperature T_b , and the X-ray luminosity L_X . From Equation 21 of Weaver et al. (1977),

$$t = \left(\frac{125}{154\pi} \right)^{-1/3} L_w^{-1/3} \rho^{1/3} R_b^{5/3} \quad (2)$$

which yields $t = 2.4 \times 10^4 \text{ yr}$. This age is younger than the estimated age of the YSOs; e.g. the molecular gas outflows from H72.97–69.39 have an associated timescale of $\approx 6.5 \times 10^4 \text{ yr}$ (Nayak et al. 2019). From t , the Weaver model predicts a bubble temperature T_b of (their Equation 37)

$$T_b = 2.07 \times 10^6 L_{36}^{8/35} n_0^{2/35} t_6^{-6/35} \text{ K}, \quad (3)$$

where $L_{36} \equiv L_w/10^{36} \text{ erg s}^{-1}$, $t_6 \equiv t/10^6 \text{ yr}$, and $n_0 = \rho/\mu m_p$ is the ambient number density. Assuming a mean molecular weight of $\mu = 1.4$ for the background gas, we find $T_b = 1.0 \times 10^7 \text{ K}$, corresponding to $kT = 0.9 \text{ keV}$. This value is statistically lower than our estimated $kT = 3.5_{-2.2}^{+32.1} \text{ keV}$ from X-ray spectral modeling (see Table 2). As the Weaver et al. (1977) model does not take into account cooling at the bubble-shell interface, it over-estimates the mass-loading of the bubble interior, leading to an under-estimate of T_b (see e.g. Eq. 45 of El-Badry et al. 2019), consistent with what we see here.

Finally, we combine the above derived quantities with X-ray emissivities calculated with yt’s X-ray emissivity⁶ calculator (Turk et al. 2011) to find an associated X-ray luminosity in the 0.5–7 keV band for the Weaver et al. (1977) model of $L_X = 3.4 \times 10^{35} \text{ erg s}^{-1}$. This value is about an order of magnitude larger than the observed L_X (see Table 2). We can get another estimate of the X-ray luminosity from the Weaver et al. (1977) model by following the derivation of Appendix B of Chu & Mac Low (1990), which takes into account the temperature and density variation in the bubble’s interior due to the evaporative mass flow in the Weaver et al. (1977) model. Using their Equation B7 we infer an X-ray luminosity of $L_X = 1.0 \times 10^{35} \text{ erg s}^{-1}$, which is still an order of magnitude larger than the observed value.

These estimates, combined with the very young age inferred from the application of the Weaver et al. (1977) model through Equation 2, indicates that there is likely

significant cooling at the wind bubble’s interface. Such cooling would both reduce the efficiency of the bubble’s expansion (Rosen et al. 2014; Lancaster et al. 2021a,b), explaining an older age, and reduce the mass-loading of the bubble from conductive evaporation (El-Badry et al. 2019), explaining a lower L_X . Numerical simulations following the formation of individual massive stars have confirmed that these effects occur early (Rosen 2022).

4.2. Comparison to Other Young Star Clusters

Diffuse X-ray emission associated with gas shock-heated by stellar wind feedback has been detected in many other young star-forming regions, including NGC 3603 (Moffat et al. 2002), the Arches Cluster (Yusef-Zadeh et al. 2002), RCW 38 (Wolk et al. 2002; Fukushima et al. 2023), M17 (Townesley et al. 2003), the Rosette Nebula (Townesley et al. 2003), Westerlund 1 (Muno et al. 2006), the Carina Nebula (Townesley et al. 2011), and 30 Doradus (Townesley et al. 2006; Lopez et al. 2011). The characteristics of these star-forming regions are shown in Table 3, spanning two orders of magnitude in bolometric luminosity L_{bol} and four orders of magnitude in L_X .

One region with a young age similar to H72.97–69.39 is the Milky Way HII region RCW 38 which is estimated to be 0.1–0.5 Myr old (Wolk et al. 2006; Fukui et al. 2016). RCW 38 has ~ 80 times lower bolometric luminosity (with $L_{\text{bol}} = 9.7 \times 10^5 L_\odot$), an order of magnitude lower X-ray luminosity (with $L_X = (1.5 \pm 0.2) \times 10^{33} \text{ erg s}^{-1}$), and a slightly higher hot gas temperature (with $kT = 4.5_{-0.9}^{+1.2} \text{ keV}$) than H72.97–69.39 (Pandey et al. 2024). The diffuse X-ray emission of RCW 38 requires both thermal and non-thermal components to fit the spectra (Wolk et al. 2002; Fukushima et al. 2023; Pandey et al. 2024), whereas the weaker signal from H72.97–69.39 does not enable us to distinguish whether both components are necessary to model the data adequately. Both H72.97–69.39 and RCW 38 demonstrate that diffuse X-rays associated with stellar winds are produced early in MSC formation.

5. CONCLUSIONS

In this work, we present new Chandra observations totaling 98 ks toward the potential superstar cluster (SSC) H72.97–69.39 in N79-South. We detect ~ 160 net, background-subtracted, broad-band X-ray counts from the $1'$ vicinity of H72.97–69.39 where five YSOs have been identified using JWST (see Figure 2). We also serendipitously detect ~ 12 net counts from another location in N79-South with three YSOs (see Figure 6). The X-ray emission is extended $\sim 10''$ in radius, much greater than the Chandra on-axis PSF, which demonstrates that diffuse hot gas is produced by stellar-wind feedback in the earliest stages of formation.

We show that the X-ray emission around H72.97–69.39 is especially hard, dominated by photons above 1.2 keV, suggesting a high hot gas temper-

⁶ See https://hea-www.cfa.harvard.edu/~jzuhone/pyxsim/xray_fields.html

Table 3. Characteristics of Star-Forming Regions with Detected Diffuse X-ray Emission

Region	Age	Radius ^a	Distance	L_{bol}	L_X	References
	(Myr)	(pc)	(kpc)	(L_{\odot})	(erg s^{-1})	
RCW 38	0.1–0.5	10	1.7	9.7×10^5	1.5×10^{33}	1, 2, 3, 4
N79	0.5	64	50	2.2×10^6	1.5×10^{34}	this work, 5, 6
NGC 3603 ^{b,c}	1	21	7.0	2.3×10^7	2.6×10^{35}	7, 8, 9, 10
Arches Cluster ^{d,e}	1–2	3.6	8.5	...	1.6×10^{34}	11
30 Doradus ^b	1–2	100	50	7.8×10^7	4.5×10^{36}	12, 13
Carina Nebula	2–3	20	2.3	2.5×10^7	1.7×10^{35}	10, 14,
Rosette Nebula	2–4	16.5	1.4	2.3×10^6	6.0×10^{32}	15, 16, 17, 18
Westerlund 1 ^f	3–4	25	4.0	2.6×10^6	3.0×10^{34}	9, 19, 20, 21

^aRadius defined by the H-alpha emission.

^b L_X corresponding to the soft-band (0.5–2.0 keV) diffuse emission.

^cRadius corresponding to the radio flux.

^dDue to extinction uncertainties toward the Galactic Center, this L_{bol} has substantial uncertainty (Clark et al. 2018).

^eRadius corresponding to the maximum extent of the diffuse X-ray emission (3.6pc×2.4pc).

^fRadius corresponding to the extent of the H I bubble.

References—(1) Rodgers et al. (1960); (2) Wolk et al. (2006); (3) Fukui et al. (2016); (4) Pandey et al. (2024); (5) Lopez et al. (2014); (6) Ochsendorf et al. (2017); (7) Balick et al. (1980); (8) Moffat et al. (2002); (9) Binder & Povich (2018); (10) Townsley et al. (2011); (11) Yusef-Zadeh et al. (2002); (12) Lopez et al. (2011); (13) Malumuth & Heap (1994); (14) Harper-Clark & Murray (2009); (15) Bruhweiler et al. (2010); (16) Celnik (1985); (17) Cox et al. (1990); (18) Townsley et al. (2003); (19) Munro et al. (2006); (20) Kothes & Dougherty (2007); (21) Dougherty et al. (2010)

ature, a large absorbing column in the region, presence of colliding-wind massive binaries, and/or contribution from a non-thermal/power-law component. The X-rays appear to be spatially anti-coincident with the ^{13}CO dense gas (Figure 4), suggesting that the hot gas is preferentially occupying the lower-density cavities and/or that X-rays are absorbed by the dense gas.

Comparison to stellar wind model predictions shows that the X-ray luminosity of H72.97–69.39 is about one order of magnitude below expected if the shock-heated gas is confined by a cool shell that heats up via thermal conduction and evaporates. This result suggest that, even this early in the MSC formation process, significant amounts of wind energy are being lost. Likely explanations are either turbulent mixing followed by radiative cooling (Rosen et al. 2014; Lancaster et al. 2021a,b) or physical leakage of the gas (Harper-Clark & Murray

2009), with the former likely playing a larger role (Lancaster et al. 2021c).

Software: CIAO (v4.15; Fruscione et al. 2006), XSPEC (v12.13.0c; Arnaud 1996)

ACKNOWLEDGMENTS

We are grateful for the helpful feedback from Marta Sewilo and the anonymous referee. Support for this work was provided by the National Aeronautics and Space Administration through Chandra Award Number GO0-21071X issued by the Chandra X-ray Center, which is operated by the Smithsonian Astrophysical Observatory for and on behalf of the National Aeronautics Space Administration under contract NAS8-03060. JR and LAL also acknowledge support through the Heising-Simons Foundation grant 2022-3533. LAL and LL gratefully acknowledges the support of the Simons Foundation.

REFERENCES

- Agertz, O., Kravtsov, A. V., Leitner, S. N., & Gnedin, N. Y. 2013, *ApJ*, 770, 25, doi: [10.1088/0004-637X/770/1/25](https://doi.org/10.1088/0004-637X/770/1/25)
- Arnaud, K. A. 1996, in *Astronomical Society of the Pacific Conference Series*, Vol. 101, *Astronomical Data Analysis Software and Systems V*, ed. G. H. Jacoby & J. Barnes, 17

- Asplund, M., Grevesse, N., Sauval, A. J., & Scott, P. 2009, *ARA&A*, 47, 481, doi: [10.1146/annurev.astro.46.060407.145222](https://doi.org/10.1146/annurev.astro.46.060407.145222)
- Balick, B., Boeshaar, G. O., & Gull, T. R. 1980, *ApJ*, 242, 584, doi: [10.1086/158493](https://doi.org/10.1086/158493)
- Binder, B. A., & Povich, M. S. 2018, *ApJ*, 864, 136, doi: [10.3847/1538-4357/aad7b2](https://doi.org/10.3847/1538-4357/aad7b2)
- Bruhweiler, F. C., Freire Ferrero, R., Bourdin, M. O., & Gull, T. R. 2010, *ApJ*, 719, 1872, doi: [10.1088/0004-637X/719/2/1872](https://doi.org/10.1088/0004-637X/719/2/1872)
- Cantó, J., Raga, A. C., & Rodríguez, L. F. 2000, *ApJ*, 536, 896, doi: [10.1086/308983](https://doi.org/10.1086/308983)
- Castor, J., McCray, R., & Weaver, R. 1975, *ApJL*, 200, L107, doi: [10.1086/181908](https://doi.org/10.1086/181908)
- Celnik, W. E. 1985, *A&A*, 144, 171
- Chevalier, R. A., & Clegg, A. W. 1985, *Nature*, 317, 44, doi: [10.1038/317044a0](https://doi.org/10.1038/317044a0)
- Choi, J., Dotter, A., Conroy, C., et al. 2016, *ApJ*, 823, 102, doi: [10.3847/0004-637X/823/2/102](https://doi.org/10.3847/0004-637X/823/2/102)
- Chu, Y.-H., & Mac Low, M.-M. 1990, *ApJ*, 365, 510, doi: [10.1086/169505](https://doi.org/10.1086/169505)
- Clark, J. S., Lohr, M. E., Najarro, F., Dong, H., & Martins, F. 2018, *A&A*, 617, A65, doi: [10.1051/0004-6361/201832826](https://doi.org/10.1051/0004-6361/201832826)
- Cox, P., Deharveng, L., & Leene, A. 1990, *A&A*, 230, 181
- Dotter, A. 2016, *ApJS*, 222, 8, doi: [10.3847/0067-0049/222/1/8](https://doi.org/10.3847/0067-0049/222/1/8)
- Dougherty, S. M., Clark, J. S., Negueruela, I., Johnson, T., & Chapman, J. M. 2010, *A&A*, 511, A58, doi: [10.1051/0004-6361/200913505](https://doi.org/10.1051/0004-6361/200913505)
- Egorov, O. V., Kreckel, K., Sandstrom, K. M., et al. 2023, *ApJL*, 944, L16, doi: [10.3847/2041-8213/acac92](https://doi.org/10.3847/2041-8213/acac92)
- El-Badry, K., Ostriker, E. C., Kim, C.-G., Quataert, E., & Weisz, D. R. 2019, *MNRAS*, 490, 1961, doi: [10.1093/mnras/stz2773](https://doi.org/10.1093/mnras/stz2773)
- Fruscione, A., McDowell, J. C., Allen, G. E., et al. 2006, in *Society of Photo-Optical Instrumentation Engineers (SPIE) Conference Series*, Vol. 6270, Society of Photo-Optical Instrumentation Engineers (SPIE) Conference Series, ed. D. R. Silva & R. E. Doxsey, 62701V, doi: [10.1117/12.671760](https://doi.org/10.1117/12.671760)
- Fukui, Y., Torii, K., Ohama, A., et al. 2016, *ApJ*, 820, 26, doi: [10.3847/0004-637X/820/1/26](https://doi.org/10.3847/0004-637X/820/1/26)
- Fukushima, A., Ezoe, Y., & Odaka, H. 2023, *PASJ*, 75, 187, doi: [10.1093/pasj/psac100](https://doi.org/10.1093/pasj/psac100)
- Gordon, K. D., Engelbracht, C. W., Rieke, G. H., et al. 2008, *ApJ*, 682, 336, doi: [10.1086/589567](https://doi.org/10.1086/589567)
- Harper-Clark, E., & Murray, N. 2009, *ApJ*, 693, 1696, doi: [10.1088/0004-637X/693/2/1696](https://doi.org/10.1088/0004-637X/693/2/1696)
- Henize, K. G. 1956, *ApJS*, 2, 315, doi: [10.1086/190025](https://doi.org/10.1086/190025)
- HIPI Collaboration, Ben Bekhti, N., Flöer, L., et al. 2016, *A&A*, 594, A116, doi: [10.1051/0004-6361/201629178](https://doi.org/10.1051/0004-6361/201629178)
- Hunter, D. A., Shaya, E. J., Holtzman, J. A., et al. 1995, *ApJ*, 448, 179, doi: [10.1086/175950](https://doi.org/10.1086/175950)
- Kothes, R., & Dougherty, S. M. 2007, *A&A*, 468, 993, doi: [10.1051/0004-6361:20077309](https://doi.org/10.1051/0004-6361:20077309)
- Kroupa, P. 2001, *MNRAS*, 322, 231, doi: [10.1046/j.1365-8711.2001.04022.x](https://doi.org/10.1046/j.1365-8711.2001.04022.x)
- Krumholz, M. R., McKee, C. F., & Bland-Hawthorn, J. 2019, *ARA&A*, 57, 227, doi: [10.1146/annurev-astro-091918-104430](https://doi.org/10.1146/annurev-astro-091918-104430)
- Kurt, C. M., & Dufour, R. J. 1998, in *Revista Mexicana de Astronomia y Astrofisica Conference Series*, Vol. 7, *Revista Mexicana de Astronomia y Astrofisica Conference Series*, ed. R. J. Dufour & S. Torres-Peimbert, 202
- Lancaster, L., Ostriker, E. C., Kim, J.-G., & Kim, C.-G. 2021a, *ApJ*, 914, 89, doi: [10.3847/1538-4357/abf8ab](https://doi.org/10.3847/1538-4357/abf8ab)
- . 2021b, *ApJ*, 914, 90, doi: [10.3847/1538-4357/abf8ac](https://doi.org/10.3847/1538-4357/abf8ac)
- . 2021c, *ApJL*, 922, L3, doi: [10.3847/2041-8213/ac3333](https://doi.org/10.3847/2041-8213/ac3333)
- Lopez, L. A., Krumholz, M. R., Bolatto, A. D., Prochaska, J. X., & Ramirez-Ruiz, E. 2011, *ApJ*, 731, 91, doi: [10.1088/0004-637X/731/2/91](https://doi.org/10.1088/0004-637X/731/2/91)
- Lopez, L. A., Krumholz, M. R., Bolatto, A. D., et al. 2014, *ApJ*, 795, 121, doi: [10.1088/0004-637X/795/2/121](https://doi.org/10.1088/0004-637X/795/2/121)
- Madden, S. C., Galliano, F., Jones, A. P., & Sauvage, M. 2006, *A&A*, 446, 877, doi: [10.1051/0004-6361:20053890](https://doi.org/10.1051/0004-6361:20053890)
- Maggi, P., Haberl, F., Kavanagh, P. J., et al. 2016, *A&A*, 585, A162, doi: [10.1051/0004-6361/201526932](https://doi.org/10.1051/0004-6361/201526932)
- Malumuth, E. M., & Heap, S. R. 1994, *AJ*, 107, 1054, doi: [10.1086/116917](https://doi.org/10.1086/116917)
- Meixner, M., Gordon, K. D., Indebetouw, R., et al. 2006, *AJ*, 132, 2268, doi: [10.1086/508185](https://doi.org/10.1086/508185)
- Moffat, A. F. J., Corcoran, M. F., Stevens, I. R., et al. 2002, *ApJ*, 573, 191, doi: [10.1086/340491](https://doi.org/10.1086/340491)
- Montillaud, J., Joblin, C., & Toubanc, D. 2013, *A&A*, 552, A15, doi: [10.1051/0004-6361/201220757](https://doi.org/10.1051/0004-6361/201220757)
- Muno, M. P., Law, C., Clark, J. S., et al. 2006, *ApJ*, 650, 203, doi: [10.1086/507175](https://doi.org/10.1086/507175)
- Nayak, O., Meixner, M., Sewilo, M., et al. 2019, *ApJ*, 877, 135, doi: [10.3847/1538-4357/ab1b38](https://doi.org/10.3847/1538-4357/ab1b38)
- Nayak, O., Hirschauer, A. S., Kavanagh, P. J., et al. 2024, *ApJ*, 963, 94, doi: [10.3847/1538-4357/ad18bc](https://doi.org/10.3847/1538-4357/ad18bc)
- Ochsendorf, B. B., Zinnecker, H., Nayak, O., et al. 2017, *Nature Astronomy*, 1, 784, doi: [10.1038/s41550-017-0268-0](https://doi.org/10.1038/s41550-017-0268-0)
- Pandey, P., Lopez, L. A., Rosen, A. L., et al. 2024, *arXiv e-prints*, arXiv:2404.19001, doi: [10.48550/arXiv.2404.19001](https://doi.org/10.48550/arXiv.2404.19001)

- Points, S. D., Long, K. S., Blair, W. P., et al. 2024, *ApJ*, 974, 70, doi: [10.3847/1538-4357/ad6766](https://doi.org/10.3847/1538-4357/ad6766)
- Rauw, G., & Nazé, Y. 2016, *Advances in Space Research*, 58, 761, doi: [10.1016/j.asr.2015.09.026](https://doi.org/10.1016/j.asr.2015.09.026)
- Rodgers, A. W., Campbell, C. T., & Whiteoak, J. B. 1960, *MNRAS*, 121, 103, doi: [10.1093/mnras/121.1.103](https://doi.org/10.1093/mnras/121.1.103)
- Rosen, A. L. 2022, *ApJ*, 941, 202, doi: [10.3847/1538-4357/ac9f3d](https://doi.org/10.3847/1538-4357/ac9f3d)
- Rosen, A. L., Lopez, L. A., Krumholz, M. R., & Ramirez-Ruiz, E. 2014, *MNRAS*, 442, 2701, doi: [10.1093/mnras/stu1037](https://doi.org/10.1093/mnras/stu1037)
- Seale, J. P., Meixner, M., Sewilo, M., et al. 2014, *AJ*, 148, 124, doi: [10.1088/0004-6256/148/6/124](https://doi.org/10.1088/0004-6256/148/6/124)
- Smith, N. 2006, *MNRAS*, 367, 763, doi: [10.1111/j.1365-2966.2006.10007.x](https://doi.org/10.1111/j.1365-2966.2006.10007.x)
- Smith, R. C., & MCELS Team. 1998, *PASA*, 15, 163, doi: [10.1071/AS98163](https://doi.org/10.1071/AS98163)
- Stevens, I. R., & Hartwell, J. M. 2003, *MNRAS*, 339, 280, doi: [10.1046/j.1365-8711.2003.06184.x](https://doi.org/10.1046/j.1365-8711.2003.06184.x)
- Townsley, L. K., Broos, P. S., Chu, Y.-H., et al. 2011, *ApJS*, 194, 16, doi: [10.1088/0067-0049/194/1/16](https://doi.org/10.1088/0067-0049/194/1/16)
- Townsley, L. K., Broos, P. S., Feigelson, E. D., et al. 2006, *AJ*, 131, 2140, doi: [10.1086/500532](https://doi.org/10.1086/500532)
- Townsley, L. K., Broos, P. S., & Povich, M. S. 2024, arXiv e-prints, arXiv:2403.16944, doi: [10.48550/arXiv.2403.16944](https://doi.org/10.48550/arXiv.2403.16944)
- Townsley, L. K., Feigelson, E. D., Montmerle, T., et al. 2003, *ApJ*, 593, 874, doi: [10.1086/376692](https://doi.org/10.1086/376692)
- Turk, M. J., Smith, B. D., Oishi, J. S., et al. 2011, *The Astrophysical Journal Supplement Series*, 192, 9, doi: [10.1088/0067-0049/192/1/9](https://doi.org/10.1088/0067-0049/192/1/9)
- Vink, J. S., de Koter, A., & Lamers, H. J. G. L. M. 2000, *A&A*, 362, 295, doi: [10.48550/arXiv.astro-ph/0008183](https://doi.org/10.48550/arXiv.astro-ph/0008183)
- . 2001, *A&A*, 369, 574, doi: [10.1051/0004-6361:20010127](https://doi.org/10.1051/0004-6361:20010127)
- Weaver, R., McCray, R., Castor, J., Shapiro, P., & Moore, R. 1977, *ApJ*, 218, 377, doi: [10.1086/155692](https://doi.org/10.1086/155692)
- Willingale, R., Starling, R. L. C., Beardmore, A. P., Tanvir, N. R., & O'Brien, P. T. 2013, *MNRAS*, 431, 394, doi: [10.1093/mnras/stt175](https://doi.org/10.1093/mnras/stt175)
- Wilms, J., Allen, A., & McCray, R. 2000, *ApJ*, 542, 914, doi: [10.1086/317016](https://doi.org/10.1086/317016)
- Wolk, S. J., Bourke, T. L., Smith, R. K., Spitzbart, B., & Alves, J. 2002, *ApJL*, 580, L161, doi: [10.1086/345611](https://doi.org/10.1086/345611)
- Wolk, S. J., Spitzbart, B. D., Bourke, T. L., & Alves, J. 2006, *AJ*, 132, 1100, doi: [10.1086/505704](https://doi.org/10.1086/505704)
- Wong, T., Hughes, A., Ott, J., et al. 2011, *ApJS*, 197, 16, doi: [10.1088/0067-0049/197/2/16](https://doi.org/10.1088/0067-0049/197/2/16)
- Yusef-Zadeh, F., Law, C., Wardle, M., et al. 2002, *ApJ*, 570, 665, doi: [10.1086/340058](https://doi.org/10.1086/340058)